

# Symmetry-enforced metal-insulator transition and topological adiabatic charge pump in sliding bilayers of threefold symmetric materials

Sergio Bravo,\* P. A. Orellana, and L. Rosales  
*Departamento de Física, Universidad Técnica Federico Santa María,  
 Av. Espana 1680, Casilla Postal 110V, Valparaíso, Chile*

(Dated: May 6, 2024)

Sliding bilayers are systems that exploit the possibility of relatively translating two monolayers along a specific direction in real space, such that different stackings could be implemented in the process. This simple approach allows for manipulating the electronic properties of layered materials similarly as in twisted multilayers. In this work, the sliding of bilayers, composed of one type of monolayer with spatial symmetry described by space group  $P\bar{3}1m$  is studied. Using a minimal tight-binding model along with symmetry analysis, we propose two effects that arise in a specific sliding direction. First, the sliding-induced control of the band gap magnitude, which produces a metal-insulator transition, is demonstrated. In addition, the potential to achieve a topological adiabatic charge pump for cyclic sliding is discussed. For each effect, we also present material implementations using first-principles calculations. Bilayer GaS is selected for the metal-insulator transition and bilayer transition metal dichalcogenide  $ZrS_2$  is found to display the topological pump effect. Both realizations show good agreement with the predictions of the model.

## I. INTRODUCTION

The advent of two-dimensional materials composed of stacked atomic layers, has opened an immense spectrum of possibilities to realize new physical effects and also novel applications based on the reduced spatial dimensionality and the associated quantum phenomena that this implies. The configuration of these systems allows for precise control of the layer-by-layer composition, such as in Van der Waals heterostructures [1, 2] and also permits an effective inclusion of external perturbations such as gating, light, and magnetic fields among others [3].

A complementary form of structural manipulation relates to the relative spatial orientation of the constituent layers. In general terms, we have two possible scenarios: relative rotation and relative translation between layers. The cases of the first group, commonly known as twisted multilayer systems, comprise the materials where some monolayers are rotated with respect to a reference state such that a fixed point in space is maintained in the process. On the other hand, when a subgroup of layers is rigidly translated relative to the rest of the constituents, a sliding process is established. In this work, we concentrate on sliding configurations for the particular case of bilayer materials.

Bilayer systems have recently been the focus of intense research that have uncovered tantalizing physical properties, such as superconductivity and correlated phases in twisted bilayer graphene [4, 5] and charge ordered phases along with Wigner crystal states in hexagonal transition-metal chalcogenides [6].

Concerning sliding bilayer systems, interfacial sliding have been realized experimentally in several TMDCs, including  $MoS_2$ ,  $MoSe_2$ ,  $WS_2$ ,  $WSe_2$  and  $WTe_2$  [7, 8]. The-

oretical studies where the implications of sliding are explored include nanoscale friction in TMDCs [9], quantum phase transitions in  $MnBi_2Te_4$  [10], circular dichroism in bilayer graphene [11] and topological effects in sliding bilayer graphene [12], twisted bilayer graphene [13, 14] and other Moiré structures [15, 16].

In this work, we explore bilayer systems composed of one monolayer type. The spatial symmetry of the monolayer is described by the space group  $P\bar{3}1m$  (#164). In turn, the symmetry of the sliding bilayer system can preserve the space group of the parent monolayer for particular stacking configurations or (in general) can decrease the symmetry to a subgroup of space group #164.

In what follows, we describe the physical consequences that sliding can produce in these bilayers. We start in section II with a generic description of the geometry of the systems in terms of space groups and we put forward a minimal tight-binding model to describe the sliding process along a particular spatial direction in terms of a single scalar parameter. This model allows us to introduce two possible effects that arise from the sliding event. Namely, a metal-insulator transition that is enforced by specific symmetry and filling constraints owing to the transformations that affect the symmetry representations in momentum space. Also, for an adiabatic cyclic sliding setting, the possibility of achieving a topological charge pump along the periodic directions of the lattice.

Guided by the model results, we present in section III a material realization for each effect employing first-principles calculations, which provides numerical support for the feasibility of the proposed phenomena. We conclude in section IV by commenting on the prospects for implementation and the possible extensions that can be put forward. Additional information complementing the results presented in the main text has been left as electronic supplementary material (SI).

---

\* sergio.bravoc@usm.cl

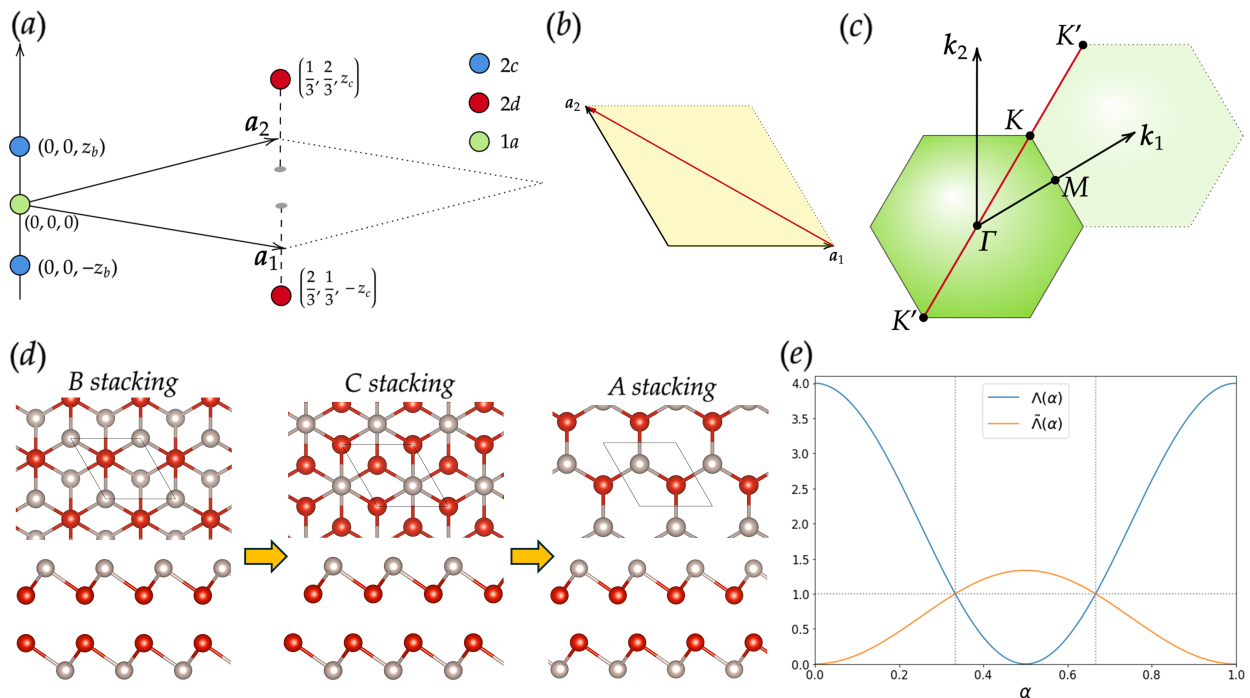


FIG. 1. (a) Unit cell and Wyckoff positions for the systems used in this work. (b) Real space displacement used for sliding. (c) Two-dimensional Brillouin zone. (d) lattice structures for the high-symmetry stackings that arise along the sliding process. (e) Variation of the tight-binding interlayer hopping parameters for the internal atoms as a function of the  $\alpha$  parameter.

## II. GEOMETRIC DESCRIPTION AND TIGHT-BINDING MODEL

### A. geometric configurations

As we mentioned above, the bilayer systems studied are conformed by a monolayer having a lattice structure described by space group (SG)  $P\bar{3}1m$  (#164). We will use this SG #164 as our reference for symmetry analysis since the bilayer stackings of interest can preserve this SG or reduce it to a subgroup of SG #164. This SG is generated by a threefold rotation around the axis perpendicular to the bilayer plane, a twofold rotation along an axis within the bilayer plane, and spatial inversion (in three dimensions). To describe all the configurations we will use a unit cell defined in three-dimensional space by the vectors  $\mathbf{a}_1 = a(1, 0, 0)$ ,  $\mathbf{a}_2 = a(-1/2, \sqrt{3}/2, 0)$ , where  $a$  is the in-plane lattice constant, as shown in FIG. 1a. We include the out-of-plane coordinate  $z$  to account for the nonzero thickness of the structures since atomic positions have nonzero  $z$ . The same unit cell is maintained for all the stackings that compose the sliding process.

We describe the sliding as a rigid relative translation between the two monolayers, characterized by a single vector in the plane formed by  $\mathbf{a}_1$  and  $\mathbf{a}_2$  vectors. In this work, we focus on particular sliding paths that contain stackings that have their symmetry described by SG #164. In general, three stackings fulfill this requirement, the features of which will be detailed below. Guided by

this high symmetry stackings (HSS), we find that six possible sliding paths contain all three HSS along the displacement. The vectors that define the direction of these paths are given by

$$\begin{aligned} & \pm (\mathbf{a}_1 + \mathbf{a}_2), \\ & \pm (\mathbf{a}_1 - \mathbf{a}_2), \\ & \pm (\mathbf{a}_1 - 2\mathbf{a}_2). \end{aligned}$$

In what follows, we will focus on one of these possible translations, namely  $\mathbf{a}_1 - \mathbf{a}_2$ , since the other alternatives do not add new features to the effects discussed in this work. The selected sliding vector is depicted in FIG. 1b. The three formerly introduced HSS will be defined in terms of a minimal lattice model where only four occupied atomic positions are used. In practical terms, we keep the bottom layer of the system fixed and change the top layer coordinates to simulate the sliding process in general. The bottom layer has coordinates (in terms of the lattice vectors  $\mathbf{a}_1, \mathbf{a}_2$ )

$$\mathbf{r}_{1,b} = (1/3, 2/3, -z_i), \mathbf{r}_{2,b} = (2/3, 1/3, -z_e) \quad (1)$$

where  $-z_i$  and  $-z_e$  denote the fractional  $z$  coordinate of the atoms in bottom monolayer, such that  $z_i$  corresponds to the top atom in the monolayer, thus being an internal atom of the bilayer and  $z_e$  corresponds to the bottom atom in the monolayer, becoming an external atom in the bilayer.

The first stacking, which we denote as stacking A, will have the top layer coordinates

$$\mathbf{r}_{1,t} = (1/3, 2/3, z_e), \mathbf{r}_{2,t} = (2/3, 1/3, z_i). \quad (2)$$

The next HSS, stacking B, possesses coordinates

$$\mathbf{r}_{1,t} = (0, 0, z_e), \mathbf{r}_{2,t} = (1/3, 2/3, z_i). \quad (3)$$

Finally, stacking C is defined as

$$\mathbf{r}_{1,t} = (2/3, 1/3, z_e), \mathbf{r}_{2,t} = (0, 0, z_i). \quad (4)$$

We can now see how these three HSS can be obtained along the sliding path. If we parameterize the relative translation of the top layer by  $\alpha(\mathbf{a}_1 - \mathbf{a}_2)$ , where  $\alpha$  is a scalar that can take values from 0 to 1, then general coordinates for the top layer can be defined by

$$\begin{aligned} \mathbf{r}_{1,t}(\alpha) &= (-\alpha, \alpha, z_e), \\ \mathbf{r}_{2,t}(\alpha) &= (1/3 - \alpha, 2/3 + \alpha, z_i). \end{aligned} \quad (5)$$

Therefore, we get the sequence of stackings B,C,A,B for  $\alpha = \{0, 1/3, 2/3, 1\}$ , respectively. The lattice structures for this sequence of stackings are pictured in FIG 1d. When  $\alpha$  takes other values, we can use the same expression in eq. (5) to describe the generic sliding stage. It is worth mentioning that all the non-HSS stackings along the paths described above belong to the SG # 12. This SG can be considered as the group of the sliding path, a concept that is known as the distortion symmetry group [17]. Coincidentally, inversion symmetry is conserved along the whole path, while the threefold symmetry is only preserved in the HSS. This symmetry breaking for general stackings is responsible for the fact that degeneracies at special points in the momentum space can be controlled in the process.

Although all the HSS belong to the same SG #164, there exist differences in the symmetry classification for each stacking within this SG. The key ingredients are the Wyckoff positions (WP) that are occupied for each configuration. A bilayer system in this SG, in the HSS with the above atomic positions, will have two possible WP,  $2c$  and  $2d$ . A schematic representation of the location of this WP in the unit cell is presented in FIG. 1a. It has to be considered that the coordinates of the WP as presented in this figure will not directly correspond with the coordinates for each HSS. In order to have a perfect match for all HSS with the coordinates of the WP we should have to redefine a new unit cell for each case. However, in our case, we conserve the same unit cell because this enables a unified treatment of the sliding by using one parameter. Thereby, we only consider the underlying feature of each WP, that is the general relation of the coordinates. For the  $2c$  WP the relation is that they have mirror symmetry about the bilayer plane and that their in-plane coordinates are the same. For the case of  $2d$  WP, the atomic positions must be connected by one of the vectors  $\pm(-1/3, 1/3, 2\tilde{z})$ , where  $\tilde{z} = z_i, z_e$ . With

Stacking	$2c$	$2d$
A	$(\frac{1}{3}, \frac{2}{3}, z_e), (\frac{2}{3}, \frac{1}{3}, -z_e)$ $(\frac{1}{3}, \frac{2}{3}, z_i), (\frac{2}{3}, \frac{1}{3}, -z_i)$	-
B	$(\frac{1}{3}, \frac{2}{3}, z_i), (\frac{1}{3}, \frac{2}{3}, -z_i)$	$(0, 0, z_e), (\frac{2}{3}, \frac{1}{3}, -z_e)$
C	$(\frac{1}{3}, \frac{2}{3}, z_e), (\frac{1}{3}, \frac{2}{3}, -z_e)$	$(0, 0, z_i), (\frac{2}{3}, \frac{1}{3}, -z_i)$

TABLE I. Identification of the Wyckoff positions for each high-symmetry stacking.

this identification, we classify the WP for the three HSS. A summary of this procedure is presented in TABLE I.

The utility of this WP identification is that it will provide a more in-depth understanding of the electronic effects derived from sliding, and will also guide the tight-binding model, which we proceed to outline next.

## B. Minimal tight-binding model

The starting point for developing the minimal model is considering that we have four atomic positions at hand. Thus, we will decorate each position with a single spinless orbital. From symmetry considerations, each atomic position belongs to a unique WP, as explained in the previous paragraph. A so-called site-symmetry group (SSG) can be associated to each WP position, which comprises the spatial symmetries that leave the WP points invariant [18]. This SSG is important since it allows classifying the atomic orbitals according to the irreducible representations (irreps) of the corresponding group [19]. Finally, when passing to the momentum space description of the system, a set of orbitals (transforming as a SSG irrep), will induce a set of irreps at every point in the Brillouin zone (BZ) [18]. This set of irreps coming from the atomic limits in real space is known as a elementary band representation (EBR) [20]. These EBRs give the symmetry content in reciprocal space and yield information on how the wavefunctions must transform along the whole BZ.

For the bilayers in this work, we have two WP, and each WP contains two single-valued irreps,  $A_1$  and  $E$ , following the notation of the Bilbao Crystallographic Center (BCS) [21]. Each irrep will induce a specific set of irreps in reciprocal space. The information of this map from WP to momentum space symmetry is presented in TABLE S1 in the SI.

More concretely, as we use four atomic orbitals, we will obtain a four-band model with a  $4 \times 4$  Hamiltonian. We will use as a basis set orbitals that transform as the  $A_1$  irrep for each WP ( $s$ ,  $p_z$  or  $d_{z^2}$ ), which we will denote and order as  $|\psi_{t,e}\rangle, |\psi_{t,i}\rangle, |\psi_{b,e}\rangle, |\psi_{b,i}\rangle$ . The first subscript indicates if the state belongs to the bottom ( $b$ ) or top ( $t$ ) layer and the second if it is associated with an internal ( $i$ ) or external ( $e$ ) site of the bilayer. The next step is to define the degree of hopping interactions that will be included in the model. To keep the parameters at a minimum, we include the first and second nearest-neighbor

(NN) intralayer interactions and two direct interlayer interactions, one among the internal atoms and the other for external atoms of the bilayer. In this manner, the Hamiltonian matrix of the system will be expressed as

$$H = \begin{bmatrix} E_e + H_{intra}^{(2,e)} & H_{intra}^{(1)} & H_{inter}^{(i)} & 0 \\ H_{intra}^{(1)*} & E_i + H_{intra}^{(2,i)} & 0 & H_{inter}^{(e)} \\ H_{inter}^{(i)*} & 0 & E_e + H_{intra}^{(2,e)} & H_{intra}^{(1)} \\ 0 & H_{inter}^{(e)*} & H_{intra}^{(1)*} & E_i + H_{intra}^{(2,i)} \end{bmatrix}, \quad (6)$$

where  $E_i$  and  $E_e$  are the onsite energies for the internal and external bilayer sites, respectively. On the other hand, each hopping matrix element can be defined in the following way. The first NN intralayer interaction  $H_{intra}^{(1)}$  takes the form

$$H_{intra}^{(1)} = t_1(e^{i\mathbf{k}\cdot\delta_1} + e^{i\mathbf{k}\cdot\delta_2} + e^{i\mathbf{k}\cdot\delta_3}), \quad (7)$$

where  $\mathbf{k}$  is the reciprocal space vector,  $t_1$  is the hopping amplitude and the  $\delta_j$  represent the first intralayer NN vectors. The second NN intralayer interactions for internal and external atoms,  $H_{intra}^{(2,\mu)}$  ( $\mu = \{e, i\}$ ), is given by

$$H_{intra}^{(2,\mu)} = t_{2,\mu}(e^{i\mathbf{k}\cdot\gamma_1} + e^{i\mathbf{k}\cdot\gamma_2} + e^{i\mathbf{k}\cdot\gamma_3}), \quad (8)$$

such that  $t_{2,\mu}$  is the hopping amplitude and the second intralayer NN vectors are denoted as  $\gamma_j$ . The interlayer hopping between internal atoms of the bilayer,  $H_{inter}^{(i)}$ , can be expressed as

$$H_{inter}^{(i)} = \Lambda_i(\alpha)e^{i\mathbf{k}\cdot\xi_1(\alpha)} + \tilde{\Lambda}_i(\alpha)(e^{i\mathbf{k}\cdot\xi_2(\alpha)} + e^{i\mathbf{k}\cdot\xi_3(\alpha)}). \quad (9)$$

In this last expression the  $\xi_j$  represent the internal interlayer NN vectors while  $\Lambda_i(\alpha)$  and  $\tilde{\Lambda}_i(\alpha)$  denote the interlayer hopping amplitude among these atoms as a function of the sliding parameter  $\alpha$ . Lastly, the interlayer interaction among the external atoms of the bilayer can be written as

$$H_{inter}^{(e)} = \Lambda_e(\alpha)e^{i\mathbf{k}\cdot\zeta_1(\alpha)} + \tilde{\Lambda}_e(\alpha)(e^{i\mathbf{k}\cdot\zeta_2(\alpha)} + e^{i\mathbf{k}\cdot\zeta_3(\alpha)}), \quad (10)$$

where  $\Lambda_e(\alpha)$  and  $\tilde{\Lambda}_e(\alpha)$  are the alpha-dependent hopping amplitudes for this interaction and the  $\zeta_j$  denote the corresponding external interlayer NN vectors.

The explicit form of all the NN vectors defined above, intralayer and interlayer, is included in the SI.

The  $\Lambda_\mu(\alpha)$  ( $\mu = i, e$ ) amplitudes vary their magnitude as the sliding is produced. It is thus necessary to establish an explicit functional form in order to obtain a parametric Hamiltonian. We model the amplitudes following

symmetry rules that are dictated from the HSS. In the first place, for the internal amplitudes, at the B stacking ( $\alpha = 0$ ),  $\Lambda_i(\alpha)$  must be maximal and  $\tilde{\Lambda}_i(\alpha)$  must be zero. In addition, for the C ( $\alpha = 1/3$ ) and A ( $\alpha = 2/3$ ) stackings,  $\Lambda_i(\alpha) = \tilde{\Lambda}_i(\alpha)$ . In the case of the external amplitudes, the conditions are that, at C stacking,  $\Lambda_e(\alpha)$  must be maximal and  $\tilde{\Lambda}_e(\alpha)$  must be zero. While for both, A and B stackings,  $\Lambda_e(\alpha) = \tilde{\Lambda}_e(\alpha)$ . Regarding the remaining (non-HSS) stackings, which interpolate between the above cases, we only impose that they give a smooth variation of the amplitudes with respect to  $\alpha$ . We propose the following modulated functional forms that meet all the above criteria.

$$\begin{aligned} \Lambda_\mu(\alpha) &= 4\lambda_\mu \cos^2(\pi\alpha - \phi_\mu), \\ \tilde{\Lambda}_\mu(\alpha) &= \frac{4}{3}\lambda_\mu \sin^2(\pi\alpha - \phi_\mu), \end{aligned} \quad (11)$$

where  $\phi_\mu = \{0, \pi/3\}$  for  $\mu = \{e, i\}$ , respectively. The  $\lambda_\mu$  scalar parameters are defined as; the internal hopping amplitude of the C and A stackings for  $\lambda_i$  and the external hopping amplitude of the A and B stackings for  $\lambda_e$ . An example of the general form of the hoppings as a function of  $\alpha$  is presented in FIG. 1e for the internal interactions. The external hoppings behave in a similar manner only with a change of phase with respect to the internal interactions. We now put into use the model developed and show how it gives raise to two effects which depend on the sliding process and also on the symmetry character of the bands.

### C. Metal-insulator transition

In the first place, we study how the sliding process can control the gap between energy bands when we connect the B stacking to the C stacking by sliding, that is when alpha takes values from 0 to  $\pi/3$ . The reason for selecting these two stackings is that they comprise the same type of WP, one  $2c$  and one  $2d$ , which will make the effect more transparent. More in detail, we analyze the symmetry content that the orbitals induce in momentum space. As we have four  $A_1$  orbitals, inspection of TABLE S1 indicates that, if the  $A_1$  orbital locates at a  $2c$  WP then the irreps induced at the high-symmetry points of the BZ correspond to the set  $(\Gamma_1^+(1) \oplus \Gamma_2^-(1), K_1(1) \oplus K_2(1), M_1^+(1) \oplus M_2^-(1))$  (we follow the notation of the BCS [21], see FIG 1c for a representation of the momentum space high symmetry points). The numbers in parenthesis denote the dimensionality of the irrep. Conversely, if the orbital is located at the  $2d$  WP, the set of irreps at the high-symmetry points will be the  $(\Gamma_1^+(1) \oplus \Gamma_2^-(1), K_3(2), M_1^+(1) \oplus M_2^-(1))$ . It can be noted that the main difference is at the  $K$  point, where for the  $2c$  WP, two 1-D irreps are possible, while for the  $2d$  WP, only one 2-D irrep is available. These two sets give all the irreps at our disposal to label the four bands of the model. For

illustrative purposes, we fix a particular order and connectivity of the irreps to set a schematic representation for the band structure. The resulting diagram will be

$$\begin{array}{ccc} \Gamma_2^-, K_2, M_2^- & & \Gamma_2^-, K_2, M_2^- \\ \Gamma_1^+ \oplus \Gamma_2^-, K_3, M_1^+ \oplus M_2^- & \rightarrow & \Gamma_1^+, K_1, M_1^+ \\ \Gamma_1^+, K_1, M_1^+ & & \Gamma_1^+ \oplus \Gamma_2^-, K_3, M_1^+ \oplus M_2^- \end{array}.$$

Here, the B stacking is represented by the left group of irreps and the C stacking corresponds to the right group of irreps. Therefore, if we, for example, set a filling of  $1/4$  such that only the lowest-lying band is occupied at B stacking, it can be immediately noted that in passing to the C stacking, a gap-closing process must take place. This is because the lowest-lying band for this case corresponds to a connected group of two bands, which for the current filling must realize a gapless phase. In summary, if there exists an adequate band filling along with the correct band ordering and symmetry, it is possible to control the bandgap of the bilayer by means of sliding, producing a metal-insulator transition. We demonstrate the effect at the tight-binding level with a band structure calculation for the B and C stackings for a particular set of model parameters. The results are shown in FIG. 2a. Note that the path used in the band plot is defined as a red line in FIG. 1c. Also, the Fermi level has been set to zero to make evident the gap closing effect due to the change in stacking. In the next section, we give a more detailed description of the sliding-induced metal-insulator transition employing first-principles methods for a material example.

#### D. Topological adiabatic charge pump

The second situation that we want to explore is related to the evolution of the polarization of the system when a complete sliding cycle is carried from  $\alpha = 0$  to  $\alpha = 1$ . It is recalled that we cover all stackings in this process. To calculate the polarization of the system for every value of the sliding parameter, we use the modern theory of polarization in terms of the Berry phase as presented for example in [22, 23]. For the sliding bilayers we treat in this work, we have a two-dimensional reciprocal space (see FIG. 1c) and in addition the sliding parameter. Thus, a three-dimensional parameter space  $(\alpha, k_x, k_y)$  is needed to analyze the polarization. The definition for component  $j$  ( $j = \{1, 2\}$ ) of the polarization, denoted as  $P_j$ , is given by [23]

$$P_j = \frac{-e}{A_{\text{cell}}} \sum_n^{\text{occ}} \frac{\bar{\phi}_{n,j}}{\pi} \mathbf{a}_j, \quad (12)$$

where  $\bar{\phi}_{n,j}$  is the Berry phase for a band  $n$  along direction  $j$  averaged over the complementary direction in reciprocal space  $l$ . Explicitly

$$\bar{\phi}_{n,j} = \frac{1}{2\pi} \int \phi_n^{k_j}(k_l) dk_l, \quad (13)$$

where  $l = \{1, 2\}$  and  $\phi_n^{k_j}(k_l)$  is the one-dimensional Berry phase along direction  $j$  for a fixed value of  $k_l$ , which is defined as [24]

$$\phi_n^{k_j}(k_l) = i \int \langle u_{n\mathbf{k}} | \partial_{k_j} u_{n\mathbf{k}} \rangle dk_j. \quad (14)$$

In this last expression  $u_{n\mathbf{k}}$  represents the unit cell periodic part of the eigenvector for the  $n$ -th band.

The calculation of the polarization as presented above can be performed separately for each value of  $\alpha$  in the interval  $[0, 1]$ . In order to study the evolution of the polarization along the sliding, we have to take into account that the set of bands under study must be isolated in energy from the rest of the bands in the spectrum for all values of  $\alpha$ . In our four-band model, the minimal set of bands that can meet this condition is a two-band subset, and for simplicity, we chose to set the filling to one-half in such a manner that only these low-lying bands contribute to the polarization. Therefore, we choose a new set of tight-binding parameters. We have checked that the low-lying bands are gapped with respect to the upper bands throughout the sliding process.

The calculation of the polarization can be numerically implemented (see the Appendix for details) from the above formulas, and a complete cycle of sliding can be studied such that  $P_j(\alpha = 0) = P_j(\alpha = 1)$ . This implies that we are analyzing a closed surface in the  $(\alpha, k_1, k_2)$ -space, and as such, we can associate a Chern number to the evolution of the polarization [23, 24] along direction  $j$ , which we denote as  $C(j)$ . The calculation of the polarization as a function of  $\alpha$  for  $j = 1$  is presented in FIG. 2b. It is evident that this two-band polarization presents a nontrivial winding. As it is well known, the Chern number can be associated with the degree of the winding that the polarization shows as a function of the external parameter [13]. Thus, for this minimal set of (two) bands, polarization winds once, and in consequence the Chern number along direction  $j = 1$  is  $C(1) = 1$ . This nonzero Chern number implies that the sliding along the special direction presented here entails a topological adiabatic process, which in principle, will allow us to observe a charge pump effect along direction  $\mathbf{a}_1$  in real space. An analogous calculation of the polarization along direction  $j = 2$  yields a Chern number of  $C(2) = -1$ , which implies a topological charge pump along the direction  $\mathbf{a}_2$ . From the results of this model, we can infer that a pair of bands that get connected for some value(s) of  $\alpha$  will contribute a Chern number with magnitude  $|C(j)| = 1$ . Then, in a system with  $N$  bands, we can expect the magnitude of the Chern number to be  $|C(j)| = N/2$ . Although spatial inversion is present in all the steps of the sliding, it is still possible to define a charge pump effect since polarization is a lattice-valued quantity and can take nonzero

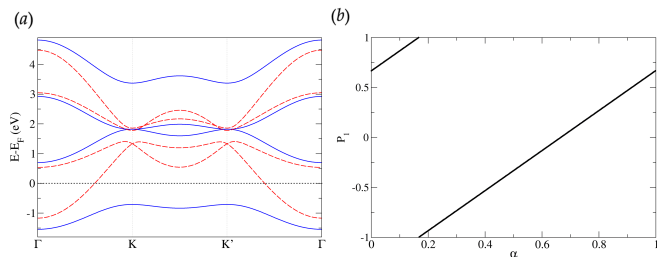


FIG. 2. (a) Band structures for the tight-binding model (used in section II C) with parameters  $E_e = 1.85$ ,  $E_i = 1.40$ ,  $t_1 = 0.63$ ,  $t_{2,e} = 0.01$ ,  $t_{2,i} = 0.023$ ,  $\lambda_i = 0.51$ ,  $\lambda_e = 0.01$ . (b) Polarization, in units of the spinless quantum of polarization, as a function of  $\alpha$  for the tight-binding model (used in section II D) using parameters  $E_e = 0.75$ ,  $E_i = -0.75$ ,  $t_1 = 1.0$ ,  $t_{2,e} = 0.09$ ,  $t_{2,i} = -0.12$ ,  $\lambda_i = -0.15$ ,  $\lambda_e = 0.01$ .

values in inversion-symmetric if the set of values respect the underlying symmetry [23]. This implies that the variation of this lattice of values with respect to the sliding parameter allows for the adiabatic charge pump effect.

Acquainted with the previous results at the tight-binding level, in the following, we are going to provide a realization of each phenomenon in representative bilayer materials.

### III. MATERIALS EXAMPLES

#### A. Metal-insulator transition in bilayer GaS

As a sample system to implement the first effect, we will use a two-layer material made of two monolayers of GaS. The lattice structure has the same configuration as the model worked previously, namely, the two Ga atoms comprise one WP, and the S atoms are located at the other WP (see FIG. 1d). The Ga atoms are the internal atoms and the S atoms form the external atom set. This material has been synthesized experimentally in layered form and present promising optoelectronic properties [25–29]. First-principles calculations were carried to simulate each step of the sliding. The details of the calculation are presented in the Appendix. To provide evidence of the control of the gap, we follow the same approach as in the tight-binding model and compute the band structure as a function of  $\alpha$ . The results are depicted for a representative array of alpha values in FIG. 3c, connecting the stacking B to stacking C. The metal-insulator transition is clearly identified and is achieved at the value of alpha  $\alpha \approx 0.2$  and remains closed until stacking C is reached.

To explore the energetic landscape of the sliding process, the energy variation,  $\Delta E$ , of the ground state for a particular stacking with respect to the stacking with lower energy (stacking B in this case) is displayed in FIG. 3b, for a complete cycle of  $\alpha$ . The cost of sliding from

B to C is about 30 meV. It can be noted that the most costly part of the cycle is to slide from C to A, whose value reaches approximately 60 meV. If the complete cycle is considered, the gap must be reopened on approaching stacking B from stacking A. This gives in principle a cyclic metal-insulator transition controlled by the sliding. Band structure calculations for a selected set of  $\alpha$  values which account for the range between C and A stackings is presented in FIG. S1 and for the range between A and B stackings in FIG. S2 in the SI.

As discussed in the context of the tight-binding model, the transition robustness stems from the symmetry and ordering of the irreps at momentum space. For the GaS case, at the B stacking the top valence band is nondegenerate and realizes the  $\Gamma_1^+, K_1, M_1^+$  band representation. The first and second conduction bands, for their part, realize the connected set  $\Gamma_1^+ \oplus \Gamma_2^-, K_3, M_1^+ \oplus M_2^-$ . Then the low energy region of GaS could be well described by the model we discussed above, when only the lowest band is filled. At B stacking, the top valence band can be considered as the bonding band of the set coming from the  $2c$  WP (Ga atoms) while the antibonding band  $\Gamma_2^-, K_2, M_2^-$ , will be higher in energy, locating above the bands coming from the  $2d$  WP. The filling restricts these  $2d$ -related bands to be antibonding conduction bands. Thereby, as the WP get reversed at stacking C, the low-lying bands will be enforced to form a connected two-band representation (having the 2-D  $K_3$  irrep at  $K$  point) which leads to a partially filled bonding band, thus protecting the transition appearance. Interestingly, the band representations induced from  $2c$  WP in the B and C stackings can be decomposed in EBRs pinned to  $1a$  WP (see 1a), which is an unoccupied WP. This indicates that these configurations realize a bilayer spinless obstructed atomic phase [18, 30, 31], which in particular is insulating at the B stacking.

#### B. Topological adiabatic charge pump in bilayer ZrS2

For the second effect, the material we select is formed by two monolayers of ZrS<sub>2</sub>, which is an experimentally synthesized structure [32, 33]. This material has been found to exhibit excellent properties for electrocatalysis and optoelectronics [34–37]. This time, the structure is formed with the S atoms occupying a twofold WP as in the previous material GaS, and the Zr atoms from each monolayer combine to conform another twofold WP. The lattice structures of the three HSS are shown in FIG. 3a. Note that in this material the stackings are labelled by considering the positions of the S atoms to maintain agreement with the previous convention. Also, the order of the stackings in the cyclic process is A,B,C,A.

In this case, the simulation of the sliding includes the ground state energy calculation along with band structure calculations to check that the complete set of valence bands remains gapped along the process. After that, a

computation of the polarization for the real space lattice directions  $\mathbf{a}_1$  and  $\mathbf{a}_2$  is carried. The details for each step in this procedure are given in the Appendix. The ground state calculations give the variation in total energy with the sliding parameter, and we display the results of these calculations in FIG. 3b.

In FIG. 3d the polarization interpolated from a set of first-principles results for particular values of  $\alpha$  (see Appendix for details) along the direction  $j = 1$  as a function of  $\alpha$  is depicted for a complete adiabatic cycle. In analogous form to the minimal model, the polarization shows a winding in the  $(\alpha, k_1, k_2)$  space. This confirms the adiabatic charge pump effect in this sliding bilayer. The Chern number extracted from the FIG. 3d plot is  $C(1) = -12$ . For bilayer  $\text{ZrS}_2$ , the valence band manifold contains 24 bands. As we previously discussed in section II C, the additive nature of the Chern number allows to predict its total magnitude by summing the contribution for each minimal set of bands (a set of two bands in these systems). In this way, as we have 24 bands then we obtain that  $|C(j)| = 24/2 = 12$ , which agrees with the first-principles result. The information of the sign of the Chern number requires additional information on the number of bands. Since it depends on the value of the  $j$  index and also on the direction of the sliding in real space.

#### IV. CONCLUSIONS

In summary, we have studied the adiabatic sliding in bilayers composed of one monolayer type with symmetries pertaining to the SG # 164. We focused on describing two effects that arise due to the sliding. In the first place, a symmetry-enforced metal-insulator transition can be produced by connecting two stacks that exchange the WP, such that the character of the bands change as we go from one stacking to the other. A minimal four-band tight-binding model can readily describe the transition, and we also show that a similar outcome arises in a bilayer of the GaS material.

Besides this effect, we found that a topological adiabatic charge pump could be established when considering a cyclic sliding process in a bilayer system that preserves its insulating character throughout the operation. This pump can be characterized by the evolution of the polarization along the real space lattice vectors as a function of the sliding parameter. The topological feature can be determined using the Chern number defined in  $(\alpha, k_1, k_2)$  space. This Chern number is related to the quantized transport properties that the system can show and scales with the number of bands. The same minimal tight-binding model could spot this effect and was also shown to appear in the bilayer form of  $\text{ZrS}_2$ , where a Chern number of  $C(j) = -12$  was encountered.

Apart from the exemplary materials, the proposed effects may occur in other materials. For instance, we have observed the metal-insulator transition in bilayer AlS and

expect it to be present in bilayer GaO since these materials have similar electronic band structure and filling as bilayer GaS (see the database associated to ref. [26] for details). In the case of the charge pump, low spin-orbit materials with a monolayer structure similar to  $\text{ZrS}_2$  are good candidates. Potential candidates are the bilayer forms of TMDCs such as  $\text{NiX}_2$ ,  $X=\{\text{S,Se}\}$ , and bilayer Mxenes such as  $\text{M}_2\text{O}_2$ ,  $M=\{\text{Sc,Ti}\}$ . As the model suggests, both phenomena are likely to be present in many systems and, as such, could be realized experimentally in device form. Also, it would be interesting to explore potential extensions of the results here presented, such for example, how magnetism can affect the ground state properties and transitions. Also, the impact of including elements with moderate to high spin-orbit coupling may be of interest. Finally, the consequences of lowering the spatial symmetry of the special stackings to structures with groups different from SG #164 will likely produce additional features associated with the symmetry-breaking process.

#### APPENDIX: COMPUTATIONAL DETAILS

The tight-binding model presented in section II was numerically implemented using the Python package PythTB [38], which can result in band structures and also has implemented the Berry phase calculation as described in [23]. For the first-principles computations, we employed the Quantum ESPRESSO code (QE) [39, 40]. The calculations contemplated first a structural relaxation for each sliding stacking considered where the force tolerance was set to 0.001 Ry/Bohr. These structures were employed to compute the ground state and the band structure for each material and for each value of the parameter  $\alpha$ . An energy cutoff of 80 Ry and a Monkhorst-Pack grid of  $10 \times 10 \times 1$  was used with the Perdew-Burke-Ernzerhof (PBE) functional [41] along with norm-conserving pseudopotentials [42] retrieved from the PseudoDojo library [43]. The energy tolerance was selected to be  $10^{-8}$  Ry.

For the polarization calculation, the internal routine of QE was used, which follows the same approach as in the tight-binding calculations [22]. For this particular step, 10 divisions for the k-line in reciprocal space yield well-converged results. The calculation of this polarization for the particular case of the  $\text{ZrS}_2$  bilayer was carried at values of  $\alpha$  following the relation  $\alpha = n/24$  with  $n$  an integer between 0 and 24. The rest of the points to construct the charge pump graph in FIG. 3d were obtained by interpolating between the calculated values always keeping the modular character of polarization, that restrict its values within 1 and -1, in units of the spin degenerate quantum of polarization.

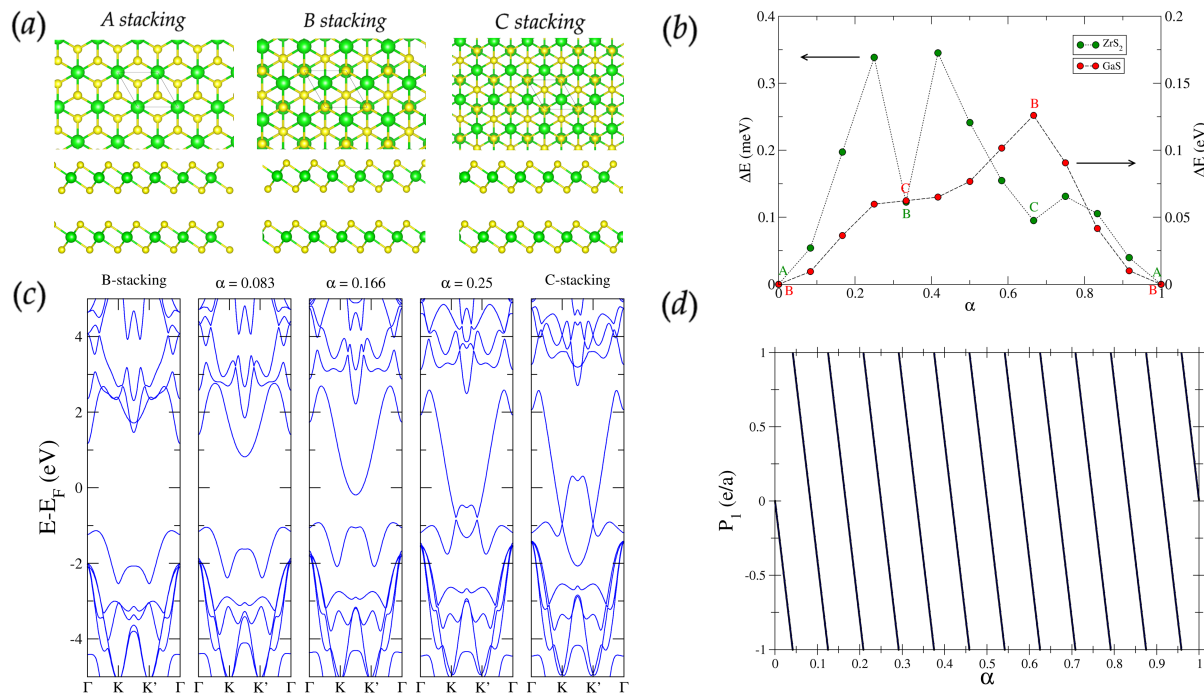


FIG. 3. (a) Lattice structures for the high-symmetry stacking in bilayer ZrS<sub>2</sub>. (b) Energy difference  $\delta E$  with respect to the lowest energy ground state for bilayer GaS and bilayer ZrS<sub>2</sub> as a function of the sliding parameter (c) Band structure for a selected set of  $\alpha$  values for bilayer GaS. (d) Polarization evolution, in units of the spinless quantum of polarization, as a function of  $\alpha$  for bilayer ZrS<sub>2</sub>.

## ACKNOWLEDGEMENTS

This work has been supported by the postdoctoral position from Universidad Técnica Federico Santa María, and Chilean FONDECYT Grant 1220700.

- 
- [1] A. K. Geim and I. V. Grigorieva, Van der waals heterostructures, *Nature* **499**, 419 (2013).
- [2] A. Castellanos-Gomez, X. Duan, Z. Fei, H. R. Gutierrez, Y. Huang, X. Huang, J. Queda, Q. Qian, E. Sutter, and P. Sutter, Van der waals heterostructures, *Nature Reviews Methods Primers* **2**, 58 (2022).
- [3] S.-J. Liang, B. Cheng, X. Cui, and F. Miao, Van der waals heterostructures for high-performance device applications: Challenges and opportunities, *Advanced Materials* **32**, 1903800 (2020).
- [4] Y. Cao, V. Fatemi, S. Fang, K. Watanabe, T. Taniguchi, E. Kaxiras, and P. Jarillo-Herrero, Unconventional superconductivity in magic-angle graphene superlattices, *Nature* **556**, 43 (2018).
- [5] Y. Cao, V. Fatemi, A. Demir, S. Fang, S. L. Tomarken, J. Y. Luo, J. D. Sanchez-Yamagishi, K. Watanabe, T. Taniguchi, E. Kaxiras, R. C. Ashoori, and P. Jarillo-Herrero, Correlated insulator behaviour at half-filling in magic-angle graphene superlattices, *Nature* **556**, 80 (2018).
- [6] K. F. Mak and J. Shan, Semiconductor moiré materials, *Nature Nanotechnology* **17**, 686 (2022).
- [7] X. Wang, K. Yasuda, Y. Zhang, S. Liu, K. Watanabe, T. Taniguchi, J. Hone, L. Fu, and P. Jarillo-Herrero, Interfacial ferroelectricity in rhombohedral-stacked bilayer transition metal dichalcogenides, *Nature Nanotechnology* **17**, 367 (2022).
- [8] C. Fox, Y. Mao, X. Zhang, Y. Wang, and J. Xiao, Stacking order engineering of two-dimensional materials and device applications, *Chemical Reviews* **124**, 1862 (2024), pMID: 38150266, <https://doi.org/10.1021/acs.chemrev.3c00618>.
- [9] A. Cammarata and T. Polcar, Overcoming nanoscale friction barriers in transition metal dichalcogenides, *Phys. Rev. B* **96**, 085406 (2017).
- [10] Y. Ren, S. Ke, W.-K. Lou, and K. Chang, Quantum phase transitions driven by sliding in bilayer mnbi<sub>2</sub>te<sub>4</sub>, *Phys. Rev. B* **106**, 235302 (2022).
- [11] Z. Addison, J. Park, and E. J. Mele, Twist, slip, and circular dichroism in bilayer graphene, *Phys. Rev. B* **100**, 125418 (2019).

- [12] Y.-W. Son, S.-M. Choi, Y. P. Hong, S. Woo, and S.-H. Jhi, Electronic topological transition in sliding bilayer graphene, *Phys. Rev. B* **84**, 155410 (2011).
- [13] Y. Zhang, Y. Gao, and D. Xiao, Topological charge pumping in twisted bilayer graphene, *Phys. Rev. B* **101**, 041410 (2020).
- [14] M. Fujimoto and M. Koshino, Moiré edge states in twisted bilayer graphene and their topological relation to quantum pumping, *Phys. Rev. B* **103**, 155410 (2021).
- [15] M. Fujimoto, H. Koschke, and M. Koshino, Topological charge pumping by a sliding moiré pattern, *Phys. Rev. B* **101**, 041112 (2020).
- [16] Y. Su and S.-Z. Lin, Topological sliding moiré heterostructure, *Phys. Rev. B* **101**, 041113 (2020).
- [17] B. K. VanLeeuwen and V. Gopalan, The antisymmetry of distortions, *Nature Communications* **6**, 8818 (2015).
- [18] B. Bradlyn, L. Elcoro, J. Cano, M. G. Vergniory, Z. Wang, C. Felser, M. I. Aroyo, and B. A. Bernevig, Topological quantum chemistry, *Nature* **547**, 298 (2017).
- [19] J. Cano and B. Bradlyn, Band representations and topological quantum chemistry, *Annual Review of Condensed Matter Physics* **12**, 225 (2021).
- [20] J. Cano, B. Bradlyn, Z. Wang, L. Elcoro, M. G. Vergniory, C. Felser, M. I. Aroyo, and B. A. Bernevig, Building blocks of topological quantum chemistry: Elementary band representations, *Phys. Rev. B* **97**, 035139 (2018).
- [21] L. Elcoro, B. Bradlyn, Z. Wang, M. G. Vergniory, J. Cano, C. Felser, B. A. Bernevig, D. Orobengoa, G. de la Flor, and M. I. Aroyo, Double crystallographic groups and their representations on the Bilbao Crystallographic Server, *Journal of Applied Crystallography* **50**, 1457 (2017).
- [22] R. D. King-Smith and D. Vanderbilt, Theory of polarization of crystalline solids, *Phys. Rev. B* **47**, 1651 (1993).
- [23] D. Vanderbilt, *Berry Phases in Electronic Structure Theory: Electric Polarization, Orbital Magnetization and Topological Insulators* (Cambridge University Press, 2018).
- [24] D. Xiao, M.-C. Chang, and Q. Niu, Berry phase effects on electronic properties, *Rev. Mod. Phys.* **82**, 1959 (2010).
- [25] R. S. Alencar, R. Longinhos, C. Rabelo, H. Miranda, B. C. Viana, A. G. S. Filho, L. G. Cançado, A. Jorio, and J. Ribeiro-Soares, Raman spectroscopy polarization dependence analysis in two-dimensional gallium sulfide, *Phys. Rev. B* **102**, 165307 (2020).
- [26] M. N. Gjerding, A. Taghizadeh, A. Rasmussen, S. Ali, F. Bertoldo, T. Deilmann, N. R. Knøsgaard, M. Kruse, A. H. Larsen, S. Manti, T. G. Pedersen, U. Petralanda, T. Skovhus, M. K. Svendsen, J. J. Mortensen, T. Olsen, and K. S. Thygesen, Recent progress of the computational 2d materials database (c2db), *2D Materials* **8**, 044002 (2021).
- [27] M. I. Zappia, G. Bianca, S. Bellani, N. Curreli, Z. Sofer, M. Serri, L. Najafi, M. Piccini, R. Oropesa-Nuñez, P. Marvan, V. Pellegrini, I. Kriegel, M. Prato, A. Cupolillo, and F. Bonaccorso, Two-dimensional gallium sulfide nanoflakes for uv-selective photoelectrochemical-type photodetectors, *The Journal of Physical Chemistry C* **125**, 11857 (2021), pMID: 34276861.
- [28] S. Ahmed, P. K. Cheng, J. Qiao, W. Gao, A. M. Saleque, M. N. Al Subri Ivan, T. Wang, T. I. Alam, S. U. Hani, Z. L. Guo, S. F. Yu, and Y. H. Tsang, Nonlinear optical activities in two-dimensional gallium sulfide: A comprehensive study, *ACS Nano* **16**, 12390 (2022), pMID: 35876327.
- [29] Y. Gutiérrez, S. Dicorato, E. Dilonardo, F. Palumbo, M. M. Giangregorio, and M. Losurdo, Stability of nanometer-thick layered gallium chalcogenides and improvements via hydrogen passivation, *ACS Applied Nano Materials* **6**, 20161 (2023).
- [30] W. A. Benalcazar, T. Li, and T. L. Hughes, Quantization of fractional corner charge in  $C_n$ -symmetric higher-order topological crystalline insulators, *Phys. Rev. B* **99**, 245151 (2019).
- [31] D.-S. Ma, K. Yu, X.-P. Li, X. Zhou, and R. Wang, Obstructed atomic insulators with robust corner modes, *Phys. Rev. B* **108**, L100101 (2023).
- [32] M. Zhang, Y. Zhu, X. Wang, Q. Feng, S. Qiao, W. Wen, Y. Chen, M. Cui, J. Zhang, C. Cai, and L. Xie, Controlled Synthesis of ZrS<sub>2</sub> Monolayer and Few Layers on Hexagonal Boron Nitride, *Journal of the American Chemical Society* **137**, 7051 (2015).
- [33] S. Mañas-Valero, V. García-López, A. Cantarero, and M. Galbiati, Raman Spectra of ZrS<sub>2</sub> and ZrSe<sub>2</sub> from Bulk to Atomically Thin Layers, *Applied Sciences* **6**, 264 (2016).
- [34] M. Mattinen, G. Popov, M. Vehkamäki, P. J. King, K. Mizohata, P. Jalkanen, J. Räisänen, M. Leskelä, and M. Ritala, Atomic layer deposition of emerging 2d semiconductors, hfs2 and zrs2, for optoelectronics, *Chemistry of Materials* **31**, 5713 (2019).
- [35] C. Tan, X. Cao, X.-J. Wu, Q. He, J. Yang, X. Zhang, J. Chen, W. Zhao, S. Han, G.-H. Nam, M. Sindoro, and H. Zhang, Recent advances in ultrathin two-dimensional nanomaterials, *Chemical Reviews* **117**, 6225 (2017), pMID: 28306244.
- [36] G. H. Han, D. L. Duong, D. H. Keum, S. J. Yun, and Y. H. Lee, van der waals metallic transition metal dichalcogenides, *Chemical Reviews* **118**, 6297 (2018), pMID: 29957928.
- [37] A. Singh and S. Pakhira, Synergistic niobium doped two-dimensional zirconium diselenide: An efficient electrocatalyst for o<sub>2</sub> reduction reaction, *ACS Physical Chemistry Au* **4**, 40 (2024).
- [38] S. Coh and D. Vanderbilt, Pythtb. <http://www.physics.rutgers.edu/pythtb>.
- [39] P. Giannozzi, S. Baroni, N. Bonini, M. Calandra, R. Car, C. Cavazzoni, D. Ceresoli, G. L. Chiarotti, M. Cococcioni, I. Dabo, *et al.*, Quantum espresso: a modular and open-source software project for quantum simulations of materials, *Journal of physics: Condensed matter* **21**, 395502 (2009).
- [40] P. Giannozzi, O. Andreussi, T. Brumme, O. Bunau, M. B. Nardelli, M. Calandra, R. Car, C. Cavazzoni, D. Ceresoli, M. Cococcioni, *et al.*, Advanced capabilities for materials modelling with quantum espresso, *Journal of physics: Condensed matter* **29**, 465901 (2017).
- [41] J. P. Perdew, K. Burke, and M. Ernzerhof, Generalized gradient approximation made simple, *Phys. Rev. Lett.* **77**, 3865 (1996).
- [42] D. R. Hamann, Optimized norm-conserving vanderbilt pseudopotentials, *Phys. Rev. B* **88**, 085117 (2013).
- [43] M. van Setten, M. Giantomassi, E. Bousquet, M. Verstraete, D. Hamann, X. Gonze, and G.-M. Rignanese, The pseudodojo: Training and grading a 85 element optimized norm-conserving pseudopotential table, *Computer Physics Communications* **226**, 39 (2018).

Electronic Supplementary Information for:  
Symmetry-enforced metal-insulator transition  
and topological adiabatic charge pump in sliding  
bilayers of threefold symmetric materials

Sergio Bravo<sup>†1</sup>, P.A. Orellana<sup>1</sup>, and L. Rosales<sup>1</sup>

<sup>1</sup>Departamento de Física, Universidad Técnica Federico Santa  
María, Valparaíso, Chile

<sup>†</sup>sergio.bravo@usm.cl

### Band representations for space group #164

WP	SSG irrep	orbitals	EBR at HSP
$2c$	$A_1$	$s, p_z, d_{z^2}$	$\Gamma_1^+ - K_1 - M_1^+$ $\Gamma_2^- - K_2 - M_2^-$
$2c$	$E$	$(p_x, p_y), (d_{xy}, d_{yz}), (d_{xy}, d_{x^2-y^2})$	$\Gamma_3^+ - K_3 - M_1^- \oplus M_2^+$ $\Gamma_3^- - K_3 - M_1^- \oplus M_1^+$
$2d$	$A_1$	$s, p_z, d_{z^2}$	$\Gamma_1^+ - K_1 - M_1^+$ $\Gamma_2^- - K_2 - M_2^-$
$2d$	$E$	$(p_x, p_y), (d_{xy}, d_{yz}), (d_{xy}, d_{x^2-y^2})$	$\Gamma_3 - K_3 - M_1^+ \oplus M_2^+$ $\Gamma_3^- - K_3 - M_1^- \oplus M_1^+$

Table S.1: elementary band representations (EBR) labelled for the space group #164 high-symmetry points (HSP) in momentum space, induced from Wyckoff positions (WP)  $2c$  and  $2d$ . The irreducible representation (irrep) in real space for each WP and the corresponding site-symmetry group (SSG) is also featured.

## Nearest-neighbors (NN) vectors for tight-binding model

Intralayer first NN

$$\delta_1 = (1/3, 2/3, \Delta_{intra}); \delta_2 = (1/3, -1/3, \Delta_{intra}); \delta_3 = (-2/3, -1/3, \Delta_{intra}).$$

Here,  $\Delta_{intra} = z_e - z_i$ , where  $z_e$  and  $z_i$  are the vertical coordinates for external and internal atoms within one of the monolayers in the bilayer.

Intralayer second NN

$$\gamma_1 = (1, 0, 0); \gamma_2 = (0, 1, 0); \gamma_3 = (1, 1, 0).$$

Interlayer internal NN

$$\xi_1 = (\alpha, -\alpha, 2z_i); \xi_2 = (\alpha, 1 - \alpha, 2z_i); \xi_3 = (-1 + \alpha, -\alpha, 2z_i).$$

Interlayer external NN

$$\zeta_1 = (2/3 + \alpha, 1/3 - \alpha, 2z_e); \zeta_2 = (-1/3 + \alpha, 1/3 + \alpha, 2z_e); \zeta_3 = (-1/3 + \alpha, -2/3 - \alpha, 2z_e).$$

## Supplementary figures

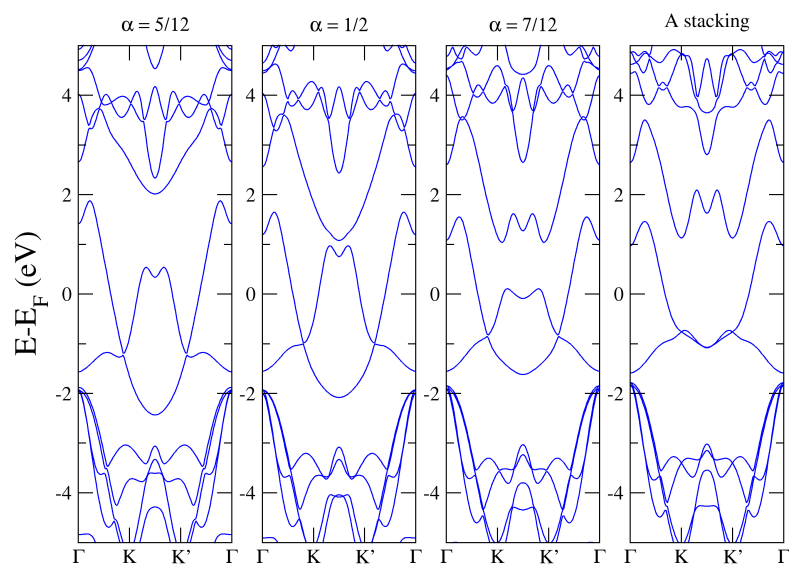


Figure S.1: Electronic band structure for values of the sliding parameter  $\alpha$  within the range between staking C ( $\alpha = 1/3$ ) and stacking A ( $\alpha = 2/3$ ).

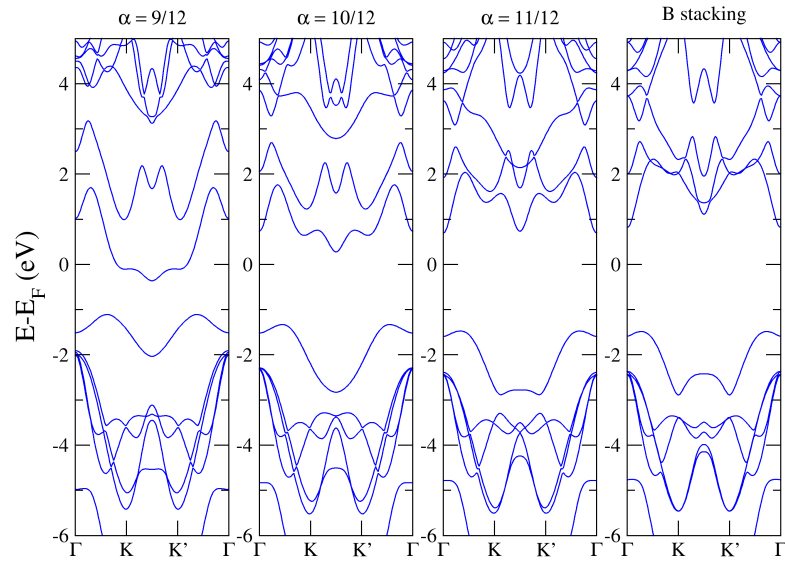


Figure S.2: Electronic band structure for values of the sliding parameter  $\alpha$  within the range between staking A ( $\alpha = 2/3$ ) and staking B ( $\alpha = 1$ ).